Journal of Manufacturing Processes 124 (2024) 1340–1348

Contents lists available at ScienceDirect

Journal of Manufacturing Processes

journal homepage: www.elsevier.com/locate/manpro

Research article

Predicting the roughness of overhanging surfaces in laser powder bed fusion via in-situ thermal imaging

Matteo Bugatti *, Bianca Maria Colosimo

Dipartimento di Meccanica, Politecnico di Milano, via La Masa 1, 20156, Milano (MI), Italy

ARTICLE INFO

Keywords:
Powder Bed Fusion
Surface roughness
In-situ monitoring
IR thermal imaging
Overhang

ABSTRACT

The production of overhanging surfaces in Laser Powder-Bed Fusion (LPBF) has long been a challenging task due to poor heat dissipation and lack of support of loose powder, resulting in surface defects and increased roughness due to dross formation and sintering. Surface quality is a critical aspect of AM mechanical components that undergo fatigue loading, as a rough surface can act as a preferential crack initiation site and lead to premature failure. Predicting the quality of the as-built surfaces could be used to identify critical areas that require rework or post-processing, or to find regions that require optimization of the process parameters to improve the final quality. The orientation of the surface itself (i.e., the degree of inclination of the surface) could be used to predict the final surface quality and will be employed as benchmarking reference throughout the work (referred to as "geometry-based" model).

This study demonstrates the effectiveness of using data mining on high-speed thermal video images to create a real-time predictive model based on "in-situ" data for estimating surface roughness (S_a) of overhanging surfaces printed at different inclinations. The results showed that the model based on "in-situ" data has a prediction accuracy that is more than 2 times higher than the one obtained with a model that is purely based on geometric data, i.e., a model that relies only on the inclination angle of the surface during the print. The proposed method is tested on different materials (AISI 316L stainless steel and AlSi10Mg) and process conditions (continuous and pulsed laser, low and high power) to show the flexibility and extended applicability of the proposed solution. The newly developed method opens new possibilities for in-situ quality control and process optimization of surface quality in Laser Powder Bed Fusion (LPBF).

1. Introduction

Laser Powder Bed Fusion (LPBF) technology has revolutionized manufacturing by providing exceptional design flexibility for producing intricate geometries. However, complex LPBF parts often exhibit sub-optimal as-built surface quality, particularly on overhanging or down-facing surfaces that lack structural support from the underlying powder substrate. This lack of support results in higher surface roughness, which can lead to defects such as dross and sintering. These defects compromise the integrity and functionality of components, potentially reducing fatigue life by up to 40% [1]. Although post-processing techniques (e.g., machining, shot peening, electrochemical polishing, etc.) can enhance surface quality, they are often costly and time-consuming, especially for geometrically complex parts [2,3]. Therefore, understanding the impact of process conditions on surface quality is crucial for developing strategies to prevent or, at least, mitigate these issues.

Extensive research has focused on the influence of process parameters and build orientations on printed surface quality in LPBF [4–7]. One critical factor is the overhang angle (i.e., the inclination of the surface measured with respect to the build direction), which significantly affects surface roughness. Higher overhang angles increase the staircase effect and hinder heat dissipation, leading to rougher surfaces. For a wide range of engineering materials such as aluminum, titanium, and nickel alloys, surface roughness (S_a) of down-facing surfaces follows a quadratic increase with the inclination angle [4]. When the inclination angle exceeds 45°, the lack of support causes the melt pool to penetrate ("sink") into the powder bed, resulting in dross formation, increased particle adhesion, and partial melting (sintering) of the powder.

The effects of laser parameters and scan strategies on surface quality have also been studied. Feng et al. [4] conducted both experimental and numerical analyses, demonstrating that increasing the volumetric energy density contributes to a substantial expansion of the melt pool, which increases its contact area with the powder bed, thus promoting the melt pool sinking mechanism described above. Other studies have highlighted the complex relationships between laser power, scan speed,

* Corresponding author.
E-mail addresses: matteo.bugatti@polimi.it (M. Bugatti), biancamaria.colosimo@polimi.it (B.M. Colosimo).

https://doi.org/10.1016/j.jmapro.2024.06.050
Received 3 May 2024; Received in revised form 5 June 2024; Accepted 22 June 2024
Available online 10 July 2024

and hatch distance [6,8,9], but these studies did not provide empirical models linking these parameters to surface roughness. Yang et al. [5] showed that the orientation of scan lines relative to overhang edges significantly impacts surface roughness, emphasizing the critical role of scan strategy. In general, researchers agree that the underlying mechanism that leads to the increase of surface roughness is intrinsically linked to the accumulation of heat near the surface of the part.

In-situ monitoring techniques have emerged as powerful tools for observing defect formation mechanisms in LPBF. These techniques can capture deviations from nominal shapes, unusual cooling dynamics, spattering, plume, and porosity [10–13]. Temperature-related metrics are particularly promising for correlating heat accumulation with surface quality. However, most studies focus on fundamental aspects such as melt pool shape and size, rather than the quality of external surfaces [14–17]. Typically, existing studies monitor the top surface, which, while convenient to observe, does not represent external surfaces facing the powder bed during printing and thus is not directly observable.

To address this gap, the present work combines ex-situ and in-situ measurements to predict the surface quality of external surfaces using an indirect monitoring approach developed on samples with varying inclinations and process conditions. Specifically, in-situ high-speed thermal imaging is employed to capture the temperature histories of overhanging surfaces printed at different inclinations. These in-situ thermal videos are then analyzed alongside ex-situ surface quality measurements to understand and model the influence of geometry and heat accumulation on the quality of external surfaces.

The proposed method is tested on different materials, namely AISI 316L and AlSi10Mg. We compare the performance of a model based on in-situ measurements (“in-situ” model) with a geometry-based model that predicts surface quality based solely on the inclination angle. The in-situ model, which relies on a flexible heat accumulation metric, proves more general and effective in predicting surface quality for new process parameter combinations. This approach could support qualification by guiding post-process operations and, ultimately, enable online optimization of the process parameters to enhance the surface quality of overhangs.

The rest of the work is organized as follows:

- Section 2 describes the experimental setup, process parameters, and data acquisition and analysis methods.
- Section 3 presents the experimental results and models linking surface quality to inclination (“geometry-based” model) and in-situ thermal signatures (“in-situ” model), including their prediction capabilities on unseen process conditions.
- Section 4 concludes the paper.

2. Materials and methods

2.1. Experimental campaigns

The primary focus of the experimental campaigns is to investigate how the surface quality is influenced by the different process conditions while monitoring how the process behaves in terms of its thermal signature. This was done to model the ex-situ surface quality measurements under different process conditions and compare the experimental factors (i.e., the different process conditions) with the in-situ temperature data as possible explanatory variables. To this end, a first set of experiments was designed to print 4 small cube-like samples considering the following factors:

- *Overhang (OH) angle*: the inclination angle of the overhang surface with respect to the build plate was varied between 0° and 50° (Fig. 1(a)).
- *Material*: the same samples were printed with AISI 316L stainless steel and AlSi10Mg aluminum powders with the same target particle size distribution (PSD) of 15–45 μm.

Table 1
Process parameters used for the experiments.

Parameter	316L	AlSi10Mg
Laser power (W)	200	200
Laser mode	Continuous wave (CW)	
Scan speed (mm/s)	900	1000
Hatch distance (mm)	0.05	0.09
Layer thickness (mm)	0.03	0.025
Hatch strategy	Meandering	Meandering
Rotation between layers (°)	90	90
Pre-heating temperature (°C)	Not set	Not set

The geometry of the printed samples is shown in Fig. 1(c).

The samples were printed on the 3D-NT LPBF system installed in the AddMe Lab facility of Politecnico di Milano (Fig. 2). The process parameters for 316L and AlSi10Mg used for the two test prints are shown in Table 1.

All process parameters were set to default, apart from the rotation between layers which was set to 90° to have a shorter, periodic sequence of 4 hatch patterns to analyze. The patterns and the hatch direction are shown in Fig. 3. The length of the scanning vectors for this sample geometry is equal to 4.8 mm at 90° and 270° rotation, while it changes at every layer for 0° and 180° rotations according to the following equation:

$$scanning\ vector\ length = 5 + Layer\,No. \cdot lt \cdot tan(OH) - 2 \cdot beam\ offset \quad [\text{mm}] \tag{1}$$

where $Layer\ No.$ is the layer number, lt is the layer thickness, OH is the surface inclination angle and $beam\ offset$ is the distance between the start/end of the vector and the edge of the part, which was set to 0.1 mm. Despite the increasing scanning vector length and print area at every layer results in a longer total time required to scan the parts, the interlayer dwell time is kept between 28–30 s for all the layers because of the constant time required for a complete recoating cycle. This allowed to avoid interaction and heat accumulation across multiple layers.

After the first set of experiments, a second experimental campaign was designed to investigate new process settings. A total of 4 additional AlSi10Mg samples were printed. In this case, the geometry was fixed (same cube-like geometry with the same OH inclination = 45°) and the samples were printed with different combinations of laser mode and power (Fig. 4):

- 1 sample printed under the default nominal process conditions (i.e., at 200 W in continuous wave (CW) mode)
- 3 samples printed in pulsed wave mode and at 3 different levels of laser power, i.e., 160 W (nominal −20%), 200 W (nominal), and 240 W (nominal +20%).

This second set of experiments allowed to expand the number of analyzed process conditions by introducing *laser power* and *laser mode* in the experimental factors.

2.2. In-situ monitoring equipment

All experiments were monitored using a high-speed medium wave infrared (MWIR) camera, the FLIR X6901sc. The camera is mounted outside a viewport placed on top of the build chamber, approximately 500 mm away from the target and inclined 30° from the vertical. The window is made of sapphire, which is characterized by a very high transmissivity for the wavelengths of interest, (transmissivity > 85% in the 2000–5000 nm range). The camera settings used to monitor all the prints are reported in Table 2.

Because of the wide range of temperatures covered during the process, the super-framing option was used to increase the dynamic range of the camera. This option consists in the acquisition of multiple

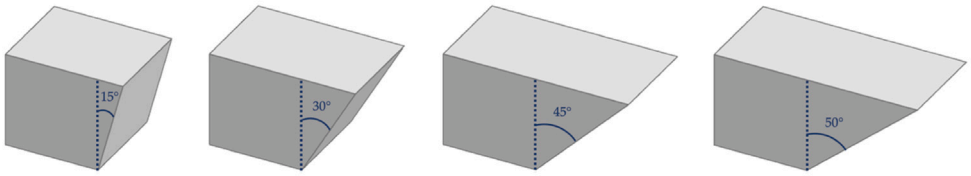

(a) Surface inclination.

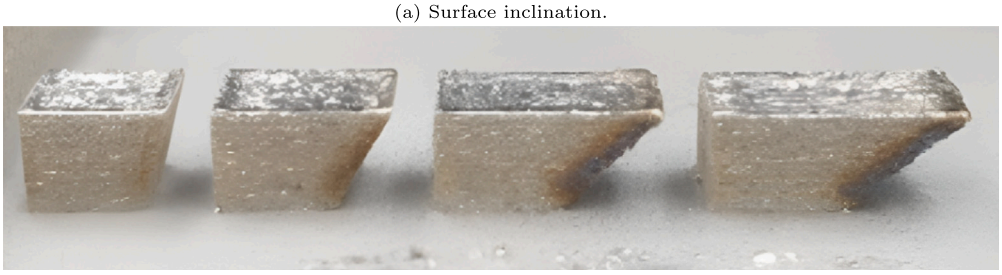

(b) AISI 316L printed samples.

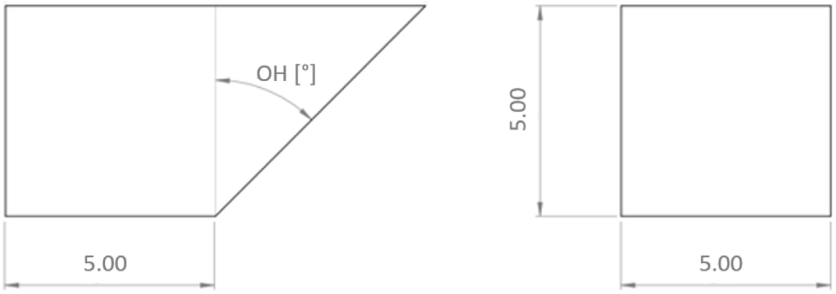

(c) Sample geometry.

Fig. 1. Sample geometry.

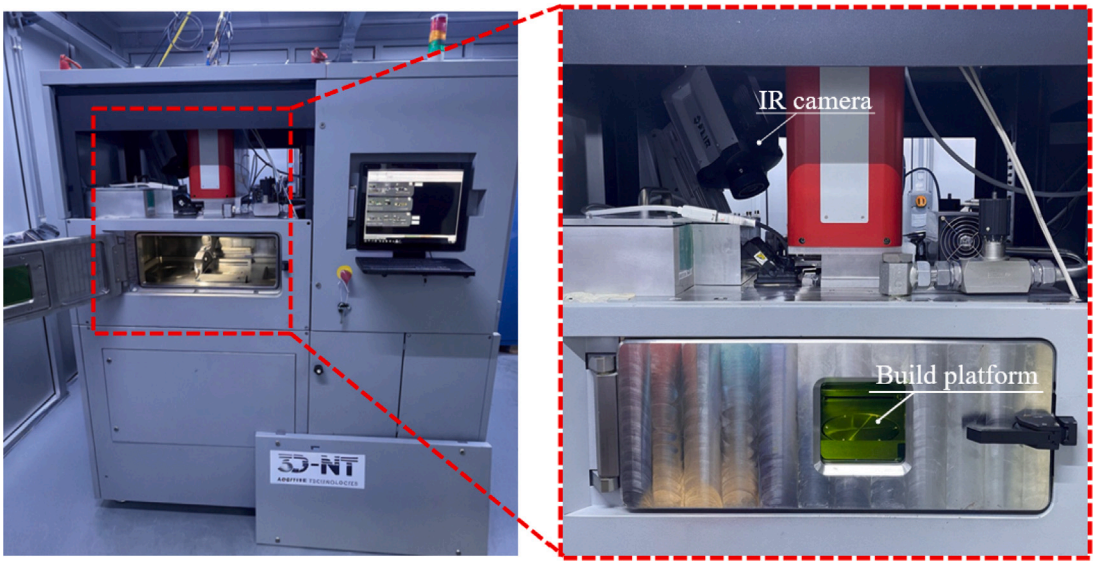

Fig. 2. 3D-NT LPBF system with the FLIR X6901sc IR camera.

consecutive frames (2 frames in this case) at different integration times, which are then combined to obtain a single image that covers a wider temperature range. The integration time of each frame is automatically set by the camera according to the temperature range of the chosen preset. This comes at the cost of a lower frame rate compared to the single preset acquisition mode, but it is necessary to capture the wide temperature range covered by the LPBF process.

A total of 4 consecutive layers were monitored for each sample at approximately 1/2 of the total height of the print. The monitored layers were chosen to be in the middle of the sample to avoid the influence

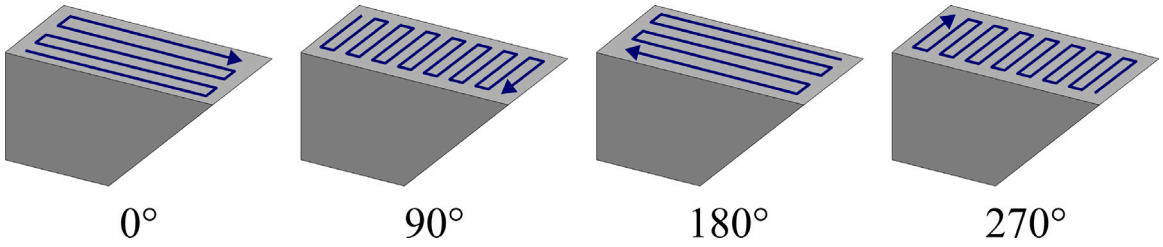

Fig. 3. Sequence of hatch patterns used for the experiments.

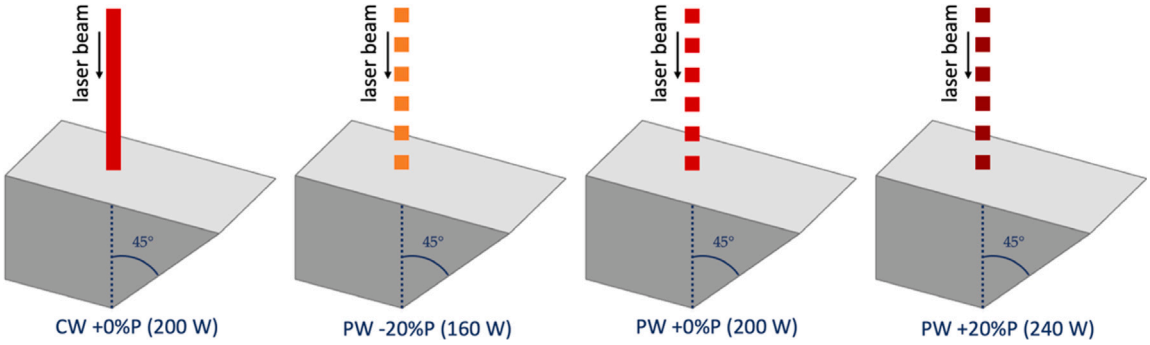

Fig. 4. Process conditions of the second experimental campaign.

Table 2
Camera settings used for the experiments.

Parameter	Value
Frame rate (fps)	667
Frame size (px)	224 × 72
Resolution (μm/px)	≈300

Table 3
Emissivity of AISI 316L and AlSi10Mg in solid state.

Material	AISI 316L	AlSi10Mg
Emissivity	0.22 [18]	0.36 [19]

of the heat sink effect of the build plate and monitor the process in a steady-state condition.

To estimate the true temperature of the body, the global equivalent emissivity, i.e., a combination of transmittance of the optical chain and emissivity of the observed materials, was measured. The transmittance was experimentally estimated following the procedure described in the ASTM E1897-97 and then multiplied by the emissivity. The emissivities of AISI 316L and AlSi10Mg in solid state were taken from literature and are reported in Table 3.

2.3. Ex-situ characterization

The external surface of the samples was characterized using a Focus Variation (FV) microscope, the Alicona InfiniteFocus. The microscope was used to reconstruct the surface topography of the down-facing surfaces, i.e., the overhangs, and the vertical surface on the opposite side of the overhang (Fig. 5).

Both the overhang and the opposite vertical surfaces were acquired with the microscope and then processed to register it with respect to a new reference system (x′y′z′, Fig. 5) and remove any unwanted tilt in the point cloud. The area was then split into 25 1 × 1 mm^2 patches over which the surface roughness S_a was computed (Fig. 6).

3. Results and discussion

The models based on the experimental factors, the in-situ acquisitions and the ex-situ characterization results are discussed in the following sections. All the models relate the surface quality measured ex-situ to either experimental factors (i.e., the surface inclination in the "geometry-based" model) or other temperature-related characteristics of the process observed via in-situ monitoring (i.e., thermal imaging results in the "in-situ" model). Depending on the availability of the chosen explanatory variables, either the full set or only a subset of the surface quality indicators extracted from the reconstructed patches was considered. Specifically, the "geometry-based" model was fitted using the full set of observations, while the "in-situ" model was fitted on a subset of observations corresponding to the monitored layers. Additional details are discussed in the following sections.

3.1. Surface roughness analysis and "geometry-based" model

Among all the possible surface quality indicators, the areal surface roughness (S_a) [20] parameter was chosen to characterize the target external surfaces. This parameter is computed as the average absolute value of the difference in height at points on a surface patch with respect to the arithmetical surface mean. The indicator is the 2-dimensional equivalent of the well-known average roughness R_a computed on 1-dimensional profiles. The S_a parameter is also commonly used in the literature to quantify the surface roughness of parts produced by LPBF [21]. Therefore, it was also selected to facilitate comparison with other works in the field. The S_a values extracted from the patches of each overhang surface were first analyzed individually to understand if the position of the patch on the surface had an influence on the surface roughness. No significant patterns or trends could be identified, therefore the individual S_a values of each patch were considered as replicates of the same process condition.

Fig. 7 shows the S_a values of the down-facing surfaces of the 316L and AlSi10Mg samples. Despite being different in absolute value, the surface roughness of the two materials show a similar trend. Up to 30° inclination, the surface roughness is still comparable with the one of the vertical surfaces. Beyond the 30° inclination, the surface

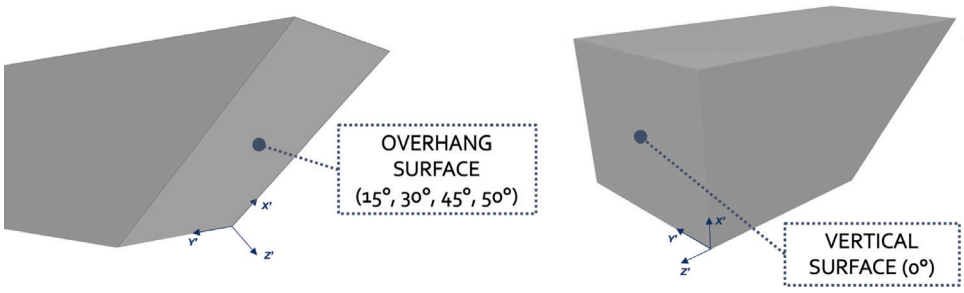

Fig. 5. Ex-situ measured surfaces.

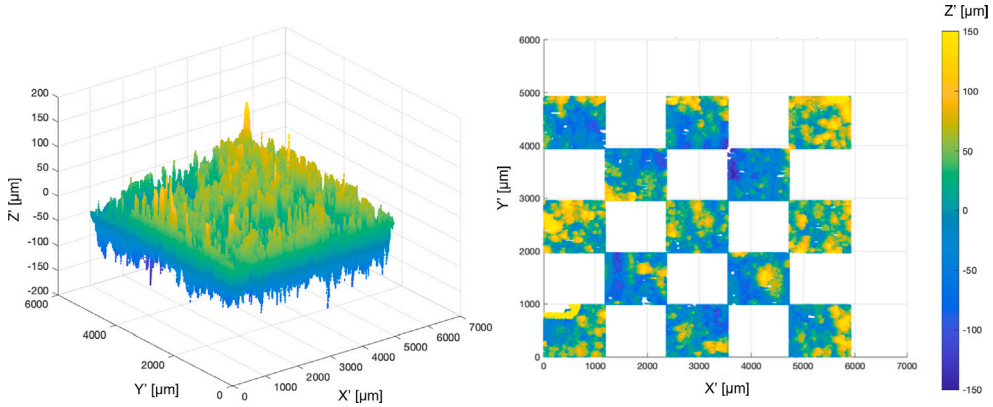

Fig. 6. Measured surface after registration (left) and patches for S_a computation (right).

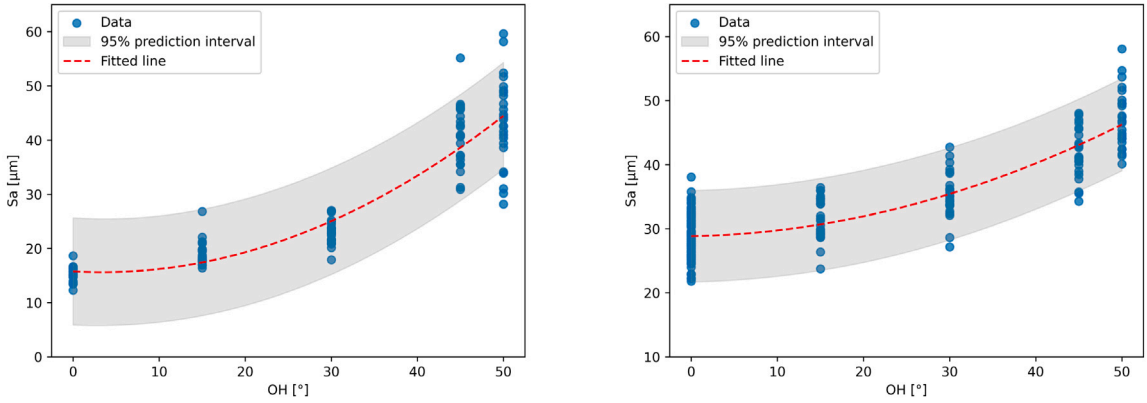

(a) S_a of 316L samples. (b) S_a of AlSi10Mg samples.

Fig. 7. S_a vs. OH models of the two materials with fitted line and 95% prediction interval.

roughness increases significantly, showing the start of what seems to be an exponential trend. This confirms that the lack of support in the overhang region induces the melt pool to sink into the loose powder bed, thus leading to higher surface roughness due to dross formation and partial powder sintering [4]. A linear regression model was fitted to the 200 surface roughness observations (i.e., 25 patches * 8 surfaces (4 with 0° inclination + 4 with 15°, 30°, 45° and 50° inclination, respectively)) to quantify the increase in surface roughness with respect to the inclination angle. The models fitted to the data are shown as red dashed lines together with their 95% prediction interval in Fig. 7. The coefficients of the two quadratic models are reported in Table 4 to predict the average S_a for any surface inclination.

The significantly different values of the intercept reflect the different surface roughness of the two materials at low inclination angles. But the same model structure, i.e., quadratic with respect to the inclination overhang angle (OH), seems to provide a good fit, regardless of the material.

3.2. Thermal images analysis and "in-situ" model

The following procedure was followed to process the thermal videos:

1. *Phase correction*: the thermal videos record the temperature history of the top surface during all the production steps. This involves the phase change of the material, i.e., from powder to liquid to solid metal. To keep into account this effect, the phase change of each pixel was tracked and the correct emissivity was assigned according to its phase.
2. *ROI selection*: the region of interest (ROI) was selected using the laser position to isolate the areas that experienced a phase change (i.e., the printed area).

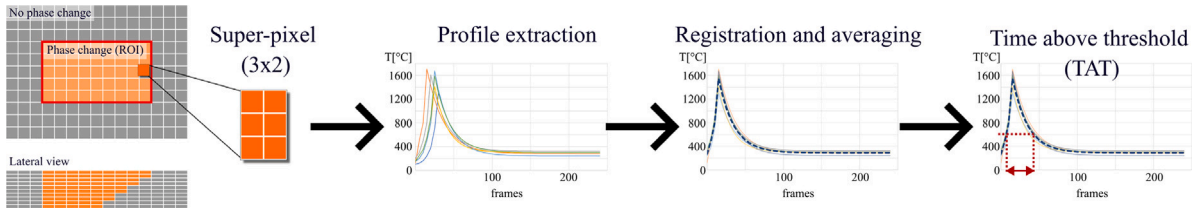

Fig. 8. High-speed IR video processing steps, from ROI definition to TAT computation.

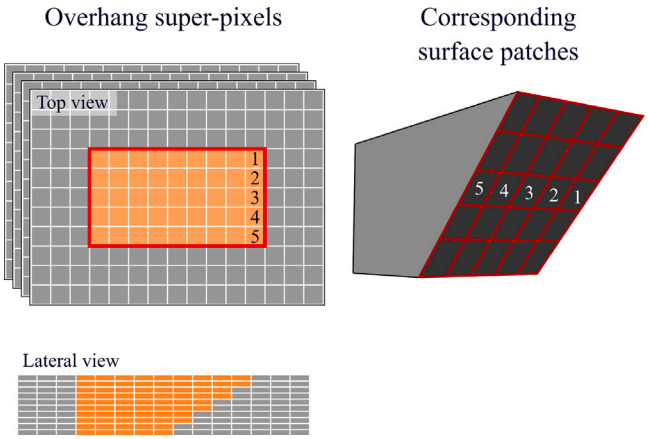

Fig. 9. Overhang edge super-pixels (left) and corresponding surface patches (right) used for the $\overline{TAT}$ vs. S_a analysis.

3. *Super-pixel*: the individual pixels along the overhang edge of the ROI were grouped into 5 "super-pixels" (3 × 2 pixels in size).
4. *Temperature profile extraction and registration*: for each super-pixel, the 6 individual temperature profiles were extracted and registered to the same reference frame to account for the small delays between hatches and then averaged to obtain a single temperature profile.
5. *Time above threshold (TAT)*: the TAT was computed from the average profile of each super-pixel. The TAT is defined as the amount of time a given temperature profile exceeds a specified threshold value. It allowed to synthetically describe the average profile while still being sensitive to the different local heat accumulation conditions within the part.

The steps are visually outlined in Fig. 8.

The choice of splitting the overhang edge of the ROI into 5 super-pixels was made for two reasons:

- *Noise reduction*: the temperature profiles of the individual pixels can be extremely noisy due to the high-frequency heating and cooling cycles induced by the laser and the process by-products (e.g., spatters, plume) affecting the reading. The registration and the averaging of all the temperature profiles in the super-pixel allow to mitigate the noise and compute a more representative TAT value, while still maintaining a good spatial resolution and being representative of the local heat accumulation near the edge of the part.
- *Correspondence with S_a patches*: the splitting of the overhang edge of the ROI into 5 regions allows to have each super-pixel match with one of the patches used for computing the S_a, as discussed in Section 3.1. The overhang edge super-pixels and the corresponding surface patches are shown in Fig. 9.

A first preliminary analysis on the TAT computed for each monitored layer showed that heat accumulation near the overhang is sensitive to the orientation of the scan strategy (Fig. 10). As discussed previously, a sequence of 4 hatch patterns was repeated for the entire build (Fig. 3), therefore, to account for the differences in heat accumulation for the 4 scan strategies, the TAT of each super-pixel was averaged over 4 consecutive layers. The average time above threshold, $\overline{TAT}$, was used for the rest of the analysis.

Table 4
Coefficients of the linear regression model fitted to the surface roughness data with the "geometry-based" model.

Material	S_a [μm]	R^2_{adj}
316L	$15.76 - 0.09 \cdot OH + 0.013 \cdot OH^2$	84.6%
AlSi10Mg	$28.82 + 0.03 \cdot OH + 0.006 \cdot OH^2$	77.2%

Table 5
Coefficients of the "in-situ-based" model fitted to the surface roughness data.

Material	S_a [μm]	R^2_{adj}
316L	$11.68 + 0.029 \cdot TAT + 0.00026 \cdot TAT^2$	96.8%
AlSi10Mg	$32.29 - 0.066 \cdot TAT + 0.00018 \cdot TAT^2$	83.0%

To set the temperature threshold for the computation of the $\overline{TAT}$, a k-fold cross-validation approach was employed. First, the $\overline{TAT}$ was extracted for different threshold values. A second order linear model with $\overline{TAT}$ as regressor was fitted on the corresponding S_a values (Eq. (2)):

$$S_a = \beta_0 + \beta_1 \cdot \overline{TAT} + \beta_2 \cdot \overline{TAT}^2 \quad (2)$$

The 5-fold cross validation was used to compare the fit of S_a vs. the $\overline{TAT}$ computed for different threshold values in terms of average mean square error (MSE). The best results were yielded when the threshold was set to 500 °C for 316L and 150 °C for AlSi10Mg. When compared to the absolute melting temperature of the two materials (i.e., 1670 K and 840 K), the two thresholds are set to approximately half the melting point of the two materials (0.46 and 0.50 respectively), indicating a possible general rule to extend this type of model to other materials with different properties.

To investigate the prediction ability of the $\overline{TAT}$ value observed in-situ and in-line as a proxy indicator of the final surface roughness, S_a, two quadratic models were fitted to the data of the first experimental campaign (Eq. (2)). In this case, 40 data points were used to fit the model (i.e., 5 patches with matching in-situ measurements * 8 surfaces (4 with 0° inclination + 4 with 15°, 30°, 45° and 50° inclination, respectively)). The models show a very good prediction ability (Fig. 11 and Table 5), with a final R^2_{adj} of 96.8% and 83.0% for 316L and AlSi10Mg, respectively.

3.3. Prediction capability for new process conditions

To evaluate the prediction capability of both the "geometry-based" and the "in-situ" models, the predictions obtained from the models fitted using only the data from the initial AlSi10Mg experimental campaign were compared to the data obtained from the second experimental campaign. This test was conducted to assess the improvement of prediction achievable when in-situ data is incorporated into the modeling process. A total of 20 S_a and TAT values (i.e., 5 patches with matching in-situ measurements * 4 surfaces printed at OH = 45°

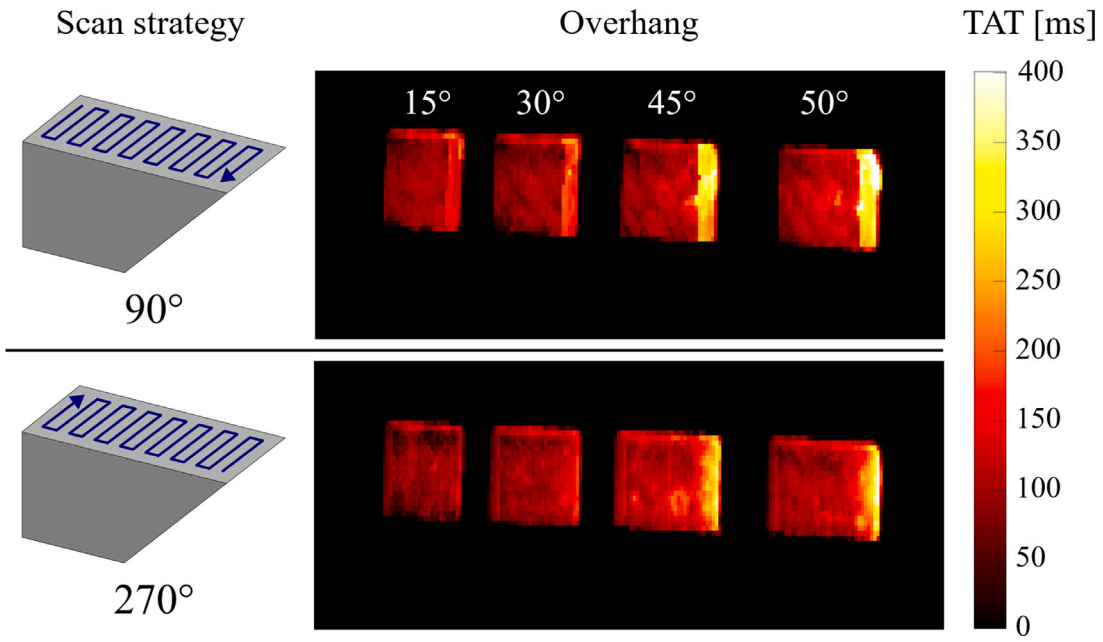

Fig. 10. Pixel-wise time above threshold map of all OH samples (*right*) computed for two different hatch patterns (90° and 270°, *left*). Heat accumulation is more extreme when the overhang area is at the end of the scan.

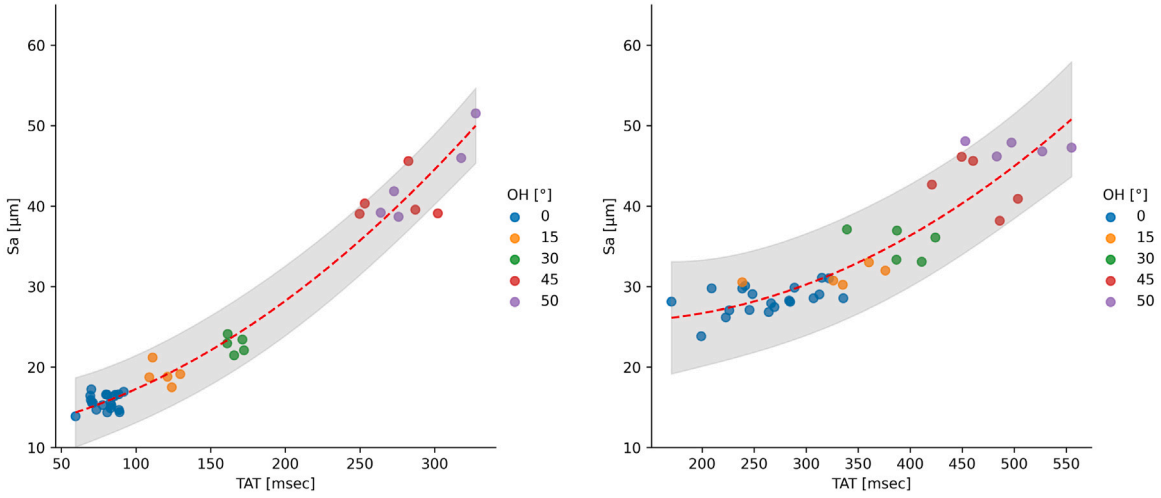

(a) 316L (b) AlSi10Mg

Fig. 11. S_a vs. $\overline{TAT}$ models of the two materials with fitted line and 95% prediction interval.

with different process parameters) were measured from the second experimental campaign and used for testing the models. The S_a data were first compared to the predictions obtained from the "geometry-based" model fitted on the data of the first experimental campaign. Fig. 12(a) shows the new observations from the second experiment plotted together with the 95% prediction band. It is clear that the "geometry-based" model, where the designed inclination angle is considered as the only explanatory variable, is not able to capture how the different process conditions influence the surface roughness. As a consequence, the same linear model to predict the surface roughness of a sample printed with different process parameters results in a significantly worse prediction capability, with a prediction root mean square error (RMSE) equal to 10 µm.

In the other case, when the "in-situ" model estimated with the first experimental campaign is used to predict new roughness data obtained with different process conditions, the prediction capability is significantly improved. In fact, unlike the overhang angle of the "geometry-based" model, the $\overline{TAT}$ used as explanatory variable in this model is sensitive to the thermal impact of the different process conditions explored with the second experimental campaign. This allows the "in-situ" model trained on the AlSi10Mg data of the first experiment to fit better the new data (Fig. 12(b)) and obtain a prediction RMSE equal to 4 µm, i.e., less than half of the prediction error obtained when only the geometry is considered in the model as relevant information to predict the surface roughness. This is also immediately noticeable from the 95% prediction intervals shown in Fig. 12: all the new observations fall within the prediction interval of the "in-situ" model, whereas several points fall outside the prediction interval of the "geometry-based" model.

Most importantly, it is interesting how the "in-situ" model seems to adjust to the new conditions without needing to be re-fitted of modified in any way. The range of $\overline{TAT}$ covered by the new observations

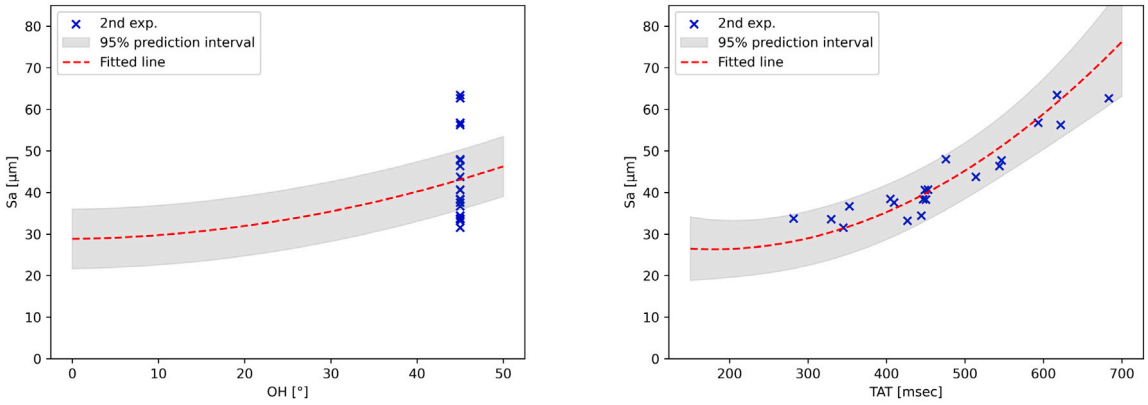

(a) "Geometry-based" model (b) "In-situ" model

Fig. 12. New experimental data plotted on the previously fitted models.

significantly extends the range over which the model was originally fitted (from $\approx [180; 550]$ to $\approx [180; 700]$), but the model appears to be just as accurate. This seems to suggest that, unlike the first "geometry-based" model, the "in-situ" model is more general as it relies on real thermal data to directly observe the true root cause of the increased surface roughness (i.e., heat accumulation). Thanks to its more general validity, it could be also used to predict the surface roughness outside of the process window used to fit the model.

The "geometry-based" model offers a good fit over the process window used for training, but it would need to be re-fitted and re-designed with additional explanatory variables to have a chance at predicting the other process conditions. While it would be possible to include other process parameters in a more complex empirical model, it is impractical to study in advance all the potential factors that might influence the heat accumulation near a surface, e.g., changes in geometry, scan order, etc., as it would require extensive experimental work.

The "in-situ" model, on the other hand, was found to provide a better fit for all the process conditions investigated in this work. This was made possible by including direct process observations in the model without forcing any other factor that fails at capturing the complex interactions between part design and process parameters that influence the heat accumulation and, ultimately, the final surface quality.

Thanks to its proven prediction capabilities, in addition to providing important insights to support surface quality control for any printed surface, the "in-situ" model can be easily envisaged as a tool for optimizing the process directly in-line, without the need to wait for the parts to be printed and measured ex-situ, thus saving time and resources.

4. Conclusions

The work presented in this paper demonstrates the potential of using in-situ high-speed thermal imaging for predicting the surface roughness of LPBF parts and compares it with an alternative model based only on geometric characteristics of the part. In particular, the following aspects have been investigated:

- *Surface roughness vs. inclination angle ("geometry-based" model).* First, the relation between surface roughness and surface inclination angle was studied for two materials, i.e., AISI 316L and AlSi10Mg. This aimed at reproducing the results reported by other authors that showed that surface roughness is strongly dependent on the inclination angle of the surface itself. Although the parameters that best fitted the data were different, for both the investigated materials it was observed a quadratic trend similar to the one found in literature.
- *A synthetic indicator called the average Time Above Threshold ($\overline{TAT}$) was introduced to assess heat accumulation via in-situ monitoring.* High-speed thermal camera data were utilized to extract the temperature profiles of pixels near the target surfaces. The profiles of adjacent pixels were grouped together into super-pixels, registered with respect to the same reference and then averaged. This allowed the calculation of the TAT indicator for all the super-pixels of each layer, i.e, the amount of time that the temperature exceeds a pre-defined temperature threshold. Cross validation was used to calibrate the threshold to the specific material being studied. The TAT values were then averaged across multiple layers to take into account the periodic behavior of the scan strategy and its influence on heat accumulation. The final $\overline{TAT}$ indicator offers a convenient way for summarizing the local heat accumulation to use it as explanatory variable to predict the final roughness on the down-facing surface.
- *Surface roughness vs. heat accumulation ("in-situ" model).* A quadratic dependency of S_a against $\overline{TAT}$ was found for both AISI 316L and AlSi10Mg and two separate models were fitted to the data of the first experimental campaign.
- *The prediction capabilities of the models were tested and compared.* The models fitted on the data of the first experiment were used to predict the surface roughness of samples printed under other process conditions (i.e., different laser power and laser mode). The "in-situ" model outperformed the "geometry-based" model in terms of prediction accuracy, with a RMSE of 4 µm vs. 10 µm on the new data.

The results demonstrate that the "in-situ" model, when compared with the simpler "geometry-based" model, is more general and capable of predicting the surface roughness even when previously unseen process parameters combinations are used. Heat accumulation has been reported as one of the main factors influencing surface quality and, since the effect of any process condition on heat accumulation is intrinsically embedded in the $\overline{TAT}$ metric used in the "in-situ" model, there is no need to fit a more complex model and incorporate new factors.

The "in-situ" model can be directly applied to monitor the status of the print and detect unwanted process drifts that affect the thermal history and influence the final surface quality of the part. This would give the possibility of supporting part qualification and guide targeted post-processing operations (if required). In addition, the "in-situ" model can be also envisaged as a tool for optimizing the process directly during the process, without the need to wait for the parts to be printed and measured ex-situ, thus reducing the time and resources required for the optimization, or even help removing the maximum surface inclination constraints, which have always been a major limitation to the design freedom in AM.

Future work will focus on exploring the boundaries and the limits of validity of the model, while testing it on other materials and process conditions.

Funding

This study was partially funded by :

- MICS (Made in Italy – Circular and Sustainable) Extended Partnership and received funding from the European Union NextGenerationEU (PIANO NAZIONALE DI RIPRESA E RESILIENZA (PNRR) – MISSIONE 4 COMPONENTE 2, INVESTIMENTO 1.3 – D.D. 1551.11-10-2022, PE00000004).

CRediT authorship contribution statement

Matteo Bugatti: Writing – review & editing, Writing – original draft, Visualization, Validation, Methodology, Investigation, Formal analysis, Data curation, Conceptualization. **Bianca Maria Colosimo:** Writing – review & editing, Supervision, Resources, Methodology, Funding acquisition, Conceptualization.

Declaration of competing interest

The authors declare that they have no known competing financial interests or personal relationships that could have appeared to influence the work reported in this paper.

References

[1] Romano S, Brückner-Foit A, Brandão A, Gumpinger J, Ghidini T, Beretta S. Fatigue properties of AlSi10Mg obtained by additive manufacturing: Defect-based modelling and prediction of fatigue strength. Eng Fract Mech 2018;187:165–89.
[2] Witkin DB, Patel DN, Helvajian H, Steffeney L, Diaz A. Surface treatment of powder-bed fusion additive manufactured metals for improved fatigue life. J Mater Eng Perform 2019;28:681–92.
[3] Urlea V, Brailovski V. Electropolishing and electropolishing-related allowances for powder bed selectively laser-melted Ti-6Al-4V alloy components. J Mater Process Technol 2017;242:1–11.
[4] Feng S, Kamat AM, Sabooni S, Pei Y. Experimental and numerical investigation of the origin of surface roughness in laser powder bed fused overhang regions. Virtual Phys. Prototyp. 2021;16(sup1):S66–84.
[5] Yang T, Liu T, Liao W, Wei H, Zhang C, Chen X, Zhang K. Effect of processing parameters on overhanging surface roughness during laser powder bed fusion of AlSi10Mg. J Manuf Process 2021;61:440–53.
[6] Koutiri I, Pessard E, Peyre P, Amlou O, De Terris T. Influence of SLM process parameters on the surface finish, porosity rate and fatigue behavior of as-built inconel 625 parts. J Mater Process Technol 2018;255:536–46.
[7] Mumtaz KA, Hopkinson N. Selective laser melting of thin wall parts using pulse shaping. J Mater Process Technol 2010;210(2):279–87. http://dx.doi.org/10.1016/j.jmatprotec.2009.09.011.
[8] Charles A, Elkaseer A, Thijs L, Hagenmeyer V, Scholz S. Effect of process parameters on the generated surface roughness of down-facing surfaces in selective laser melting. Appl Sci 2019;9(6):1256.
[9] Fox JC, Moylan SP, Lane BM. Effect of process parameters on the surface roughness of overhanging structures in laser powder bed fusion additive manufacturing. Procedia Cirp 2016;45:131–4.
[10] Grasso M, Remani A, Dickins A, Colosimo BM, Leach RK. In-situ measurement and monitoring methods for metal powder bed fusion: an updated review. Meas Sci Technol 2021;32(11):112001.
[11] Colosimo BM, Garghetti F, Pagani L, Grasso M. A novel method for in-process inspection of lattice structures via in-situ layerwise imaging. Manuf. Lett. 2022;32:67–72.
[12] Bugatti M, Colosimo BM. Towards real-time in-situ monitoring of hot-spot defects in L-PBF: a new classification-based method for fast video-imaging data analysis. J Intell Manuf 2022;33(1):293–309.
[13] Colosimo BM, Pagani L, Grasso M. Modeling spatial point processes in video-imaging via Ripley's K-function: an application to spatter analysis in additive manufacturing. J Intell Manuf 2022;1–19.
[14] Kolb T, Elahi R, Seeger J, Soris M, Scheitler C, Hentschel O, Tremel J, Schmidt M. Camera signal dependencies within coaxial melt pool monitoring in laser powder bed fusion. Rapid Prototyp. J. 2020;26(1):100–6.
[15] Vasileska E, Demir AG, Colosimo BM, Previtali B. A novel paradigm for feedback control in LPBF: layer-wise correction for overhang structures. Adv. Manuf. 2022;10(2):326–44.
[16] Foster S, Carver K, Dinwiddie R, List F, Unocic K, Chaudhary A, Babu S. Process-defect-structure-property correlations during laser powder bed fusion of alloy 718: role of in situ and ex situ characterizations. Metall Mater Trans A 2018;49:5775–98.
[17] Mohr G, Altenburg SJ, Ulbricht A, Heinrich P, Baum D, Maierhofer C, Hilgenberg K. In-situ defect detection in laser powder bed fusion by using thermography and optical tomography—comparison to computed tomography. Metals 2020;10(1):103.
[18] Mohr G, Nowakowski S, Altenburg SJ, Maierhofer C, Hilgenberg K. Experimental determination of the emissivity of powder layers and bulk material in laser powder bed fusion using infrared thermography and thermocouples. Metals 2020;10(11):1546.
[19] Dai D, Gu D. Effect of metal vaporization behavior on keyhole-mode surface morphology of selective laser melted composites using different protective atmospheres. Appl. Surf. Sci. 2015;355:310–9.
[20] ISO. ISO 25178-2:2021, geometrical product specifications (GPS) — Surface texture: Areal part 2: Terms, definitions and surface texture parameters. 2021.
[21] Townsend A, Senin N, Blunt L, Leach R, Taylor J. Surface texture metrology for metal additive manufacturing: a review. Precis Eng 2016;46:34–47.